Entanglement-enhanced synchronous differential comparison

Deshui Yu,[1] Jingbiao Chen,[2,*] and Shougang Zhang[1,3,†]
[1]*National Time Service Center, Chinese Academy of Sciences, Xi'an 710600, China*
[2]*State Key Laboratory of Advanced Optical Communication Systems and Networks, Institute of Quantum Electronics, School of Electronics, Peking University, Beijing 100871, China*
[3]*University of Chinese Academy of Sciences, Beijing 100049, China*

(Received 15 January 2023; revised 19 April 2023; accepted 20 April 2023; published 27 April 2023)

Quantum entanglement of atoms enables precision measurement and frequency metrology beyond the standard quantum limit that is imposed by the quantum projection noise. Here we propose employing entangled atoms in the synchronous differential measurement to enhance the detection sensitivity of spatially dependent frequency shift. Two ways of engineering entangled atoms are studied. The synchronous comparison between two pixels within an entangled atomic cloud leads to a sensitivity enhancement factor of 1.4 over the standard quantum limit. The sensitivity enhancement becomes saturated for a large number of atoms. In contrast, the synchronous comparison between two independent pixels that are individually composed of entangled atoms allows for a strong sensitivity enhancement by a factor of, for example, about 10 with 10^3 entangled atoms in each pixel, corresponding to a reduction of the averaging time by a factor of about 10^2. A large atom number may further elevate the sensitivity. Our work paves the way towards the entanglement-enhanced detection of gravitational redshift by means of the *in situ* imaging spectroscopy.

DOI: 10.1103/PhysRevA.107.043120

I. INTRODUCTION

Optical atomic clocks have achieved fractional frequency instabilities and systematic uncertainties at the 10^{-18} level [1–6], towards a redefinition of the SI second based upon optical transitions in atoms. The frequency comparison between two clocks lies at the heart of various applications in precision measurement and sensing on, for instance, the variation of fundamental constants such as the proton-to-electron mass ratio and the fine structure constant [7,8], the gravity potential difference between remote locations (i.e., relativistic geodesy [9–11]), and the interactions between atoms [12–14]. Recently, the robust comparison between two transportable optical lattice clocks has resulted in the most precise ground-based measurement of the gravitational redshift [15].

Thus far, the frequency instabilities of most optical clocks are still limited by the Dick effect [16], which arises from the down-conversion of the frequency noise in local lasers that are used to periodically interrogate atoms. A great deal of effort has been paid to suppress the local oscillator noise. It has been demonstrated that placing high-finesse optical resonators, to which local oscillators are prestabilized, in the cryogenic environment can vastly reduce their statistical Brownian thermal noise [17,18]. The resultant linewidths of prestabilized lasers may reach the millihertz level with a coherence time of up to 50 s and a fractional frequency instability of 4×10^{-17} at the averaging time of 1 s [19]. Nevertheless, complex laser-prestabilization measures add the significant complexity and volume to the clock setup.

In many practical applications, the absolute frequency measurement of optical clocks is unnecessary. Employing the synchronous differential comparison enables the cancellation of local oscillator noise [20,21] and reaching the standard quantum limit that is imposed by the quantum projection noise [22]. In particular, the synchronous clock comparison benefits from the long atom-atom coherence time (in principle, up to 10^2 s) and has demonstrated a fractional frequency uncertainty at the 10^{-21} level after about 10^2 hours of averaging [23]. Such an unprecedented precision can resolve the gravitational redshift between two clocks that are spatially separated at the submillimeter scale [24], offering new opportunities for testing fundamental physics. However, the long averaging time prevents the synchronous comparison from detecting relatively fast physical processes.

It has been pointed out that the standard quantum limit of the clock frequency instability may be overcome using entangled (correlated) atoms [25–27]. An optical lattice clock with hundreds of entangled atoms can shorten the averaging time by approximately three times, compared to the one with independent atoms [28]. Combining the local-oscillator-noise cancellation in the synchronous comparison and the entanglement-enhanced sensitivity beyond the standard quantum limit potentially advances the timekeeping precision and stimulates various scientific applications such as tests of fundamental physics [29] and the gravitational-wave detection [30].

In this work, we theoretically explore the application of entangled atoms in the synchronous differential comparison. We focus on the *in situ* imaging spectroscopy of a lattice-trapped

*jbchen@pku.edu.cn
†szhang@ntsc.ac.cn

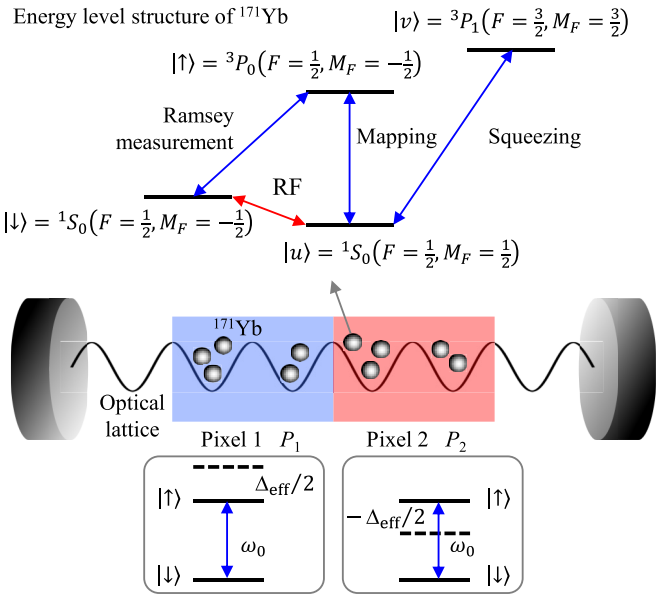

FIG. 1. Schematic of synchronous differential comparison. An ensemble of ^{171}Yb atoms is trapped in a one-dimensional optical lattice that is formed by a standing wave in an optical cavity. The atomic cloud is divided into two pixels with the same atom number N. Each atom is composed of $|\downarrow\rangle = (6s^2)\ {}^1S_0(F=\frac{1}{2}, M_F=-\frac{1}{2})$ and $|\uparrow\rangle = (6s6p)\ {}^3P_0(F=\frac{1}{2}, M_F=-\frac{1}{2})$ states. The auxiliary $|u\rangle = (6s^2)\ {}^1S_0(F=\frac{1}{2}, M_F=\frac{1}{2})$ and $|v\rangle = (6s6p)\ {}^3P_1(F=\frac{3}{2}, M_F=\frac{3}{2})$ states are used to create entangled atoms. The spatial shifts of two pixels are $\Delta_{\rm eff}/2$ and $-\Delta_{\rm eff}/2$, respectively.

atomic cloud that is divided into two pixels. For each pixel containing 10^3 atoms, the entanglement of atoms enhances the spatial-shift sensitivity by a factor of about 10 and significantly shortens the averaging time of the synchronous measurement. Increasing the atom number further raises the metrological gain. The recent atom-optical technologies allow for testing the predictions obtained in this study.

II. PHYSICAL SYSTEM

Figure 1 illustrates the schematic diagram of the physical system. ^{171}Yb atoms are tightly confined in a one-dimensional magic-wavelength (759 nm) optical lattice that is formed by a standing wave in an optical cavity [31]. The atomic cloud is divided into two groups, corresponding to two pixels in the *in situ* imaging spectroscopy [32]. We assume that two pixels contain the same number N of atoms. Each atom is modeled as a spin composed of the clock $|\downarrow\rangle = (6s^2)\ {}^1S_0(F=\frac{1}{2}, M_F=-\frac{1}{2})$ and $|\uparrow\rangle = (6s6p)\ {}^3P_0(F=\frac{1}{2}, M_F=-\frac{1}{2})$ states with the transition frequency of $\omega_0 = 2\pi\times 519$ THz. Other atomic levels and transitions shown in Fig. 1 are used for creating entangled atoms (see below). We neglect the spontaneous decay of spins since the timescale of interest in this work is much shorter than the natural lifetime (over 16 s [33]) of the $|\uparrow\rangle$ state.

The sub-Hilbert space for the kth ($k = 1, 2$) pixel is spanned by the collective spin basis $|J_k, M_k\rangle$ (i.e., the exchange-symmetric Dicke manifold), where $J_k = \frac{N}{2}$ denotes the total angular momentum and M_k corresponds to the projection. The angular momentum vector operator for the kth pixel is written as $\hat{\mathbf{J}}_k = \sum_{\mu=x,y,z} \hat{J}_{\mu,k}\hat{\mathbf{e}}_\mu$ with $\hat{\mathbf{J}}_k^2\,|J_k, M_k\rangle = J_k(J_k+1)\,|J_k, M_k\rangle$ and $\hat{J}_{z,k}\,|J_k, M_k\rangle = M_k\,|J_k, M_k\rangle$. The Hilbert space for the entire spin system is then spanned by $|J_1, M_1; J_2, M_2\rangle$, which can be simplified as $|M_1, M_2\rangle$. In the kth pixel, the spin population in $|\uparrow\rangle$ is given by $P_k = \langle\hat{P}_k\rangle = \langle\psi|\,\hat{P}_k\,|\psi\rangle$ with the projection operator $\hat{P}_k = \hat{J}_{z,k} + \frac{N}{2}$ and the system state ψ. The total projection operator is written as $\hat{P} = \hat{P}_1 + \hat{P}_2$ and $\hat{P}_d = \hat{P}_2 - \hat{P}_1$ corresponds to the projection operator for the population difference between two pixels.

The spin system experiences the extra spatially dependent frequency shifts that may be caused by, for example, the residual magnetic field gradient, the lattice-induced shifts, and the gravitational redshift. We assume that the inhomogeneity of spins within each pixel is negligible due to the small pixel size. By contrast, in order to model the relative frequency difference between two pixels, the effective spatial frequency shifts $\pm\Delta_{\rm eff}/2$ are introduced to two pixels, respectively (see Fig. 1).

We numerically simulate the Ramsey measurement. The spin system is initially prepared in $\psi_0 = |M_1 = -\frac{N}{2}, M_2 = -\frac{N}{2}\rangle$, i.e., all spins are in $|\downarrow\rangle$. Two light $\frac{\pi}{2}$-pulses are successively applied to excite spins. The gap time between two pulses is T and the phase difference between two pulses is ϕ. The populations of two pixels in $|\uparrow\rangle$, P_1 and P_2, are then measured and the population difference $P_d = \langle\hat{P}_d\rangle$ is computed. The mathematical treatment of the Ramsey measurement is listed in Appendix A.

III. INDEPENDENT SPINS

For the system composed of independent spins, the dependence of Ramsey excitation fractions of two pixels on the phase ϕ are expressed as

$$\frac{P_1}{N} = \frac{1}{2} + \frac{C}{2}\cos\left(\phi + \frac{\Delta_{\rm eff}T}{2}\right), \tag{1a}$$

$$\frac{P_2}{N} = \frac{1}{2} + \frac{C}{2}\cos\left(\phi - \frac{\Delta_{\rm eff}T}{2}\right). \tag{1b}$$

Due to the absence of the spin decay, the fringe contrast C is equal to unity. We make the parametric plot that graphs P_1 and P_2 on a coordinate system. The plot exhibits an ellipse with the lengths of major and minor axes of $2a$ and $2b$, respectively [see Figs. 2(a) and 2(b)]. Varying the spatial-shift-induced phase $\Delta_{\rm eff}T$ changes the ellipticity $e = b/a$ [see Fig. 2(c)]. The parametric plot becomes a circle, i.e., $e = 1$, when $\Delta_{\rm eff}T = \frac{\pi}{2}$. The orientation angle of the ellipse, i.e., the angle of the semimajor axis that is measured counterclockwise from the positive horizontal axis, is equal to $\frac{\pi}{4}$ or $\frac{3\pi}{4}$, depending on if $\Delta_{\rm eff}T$ is less than $\frac{\pi}{2}$.

We are interested in detecting the small spatial shift $\Delta_{\rm eff}$. In the limit of $\Delta_{\rm eff}T \sim 0$, Eq. (1) leads to

$$\Delta_{\rm eff} = \frac{2P_d}{NT\sin\phi}. \tag{2}$$

Thus, one may evaluate $\Delta_{\rm eff}$ through measuring the Ramsey excitation difference P_d between two pixels. Usually, the phase difference between two light $\frac{\pi}{2}$-pulses is set as $\phi = \frac{\pi}{2}$. Then, the uncertainty $\sigma(\Delta_{\rm eff})$ of the spatial-shift

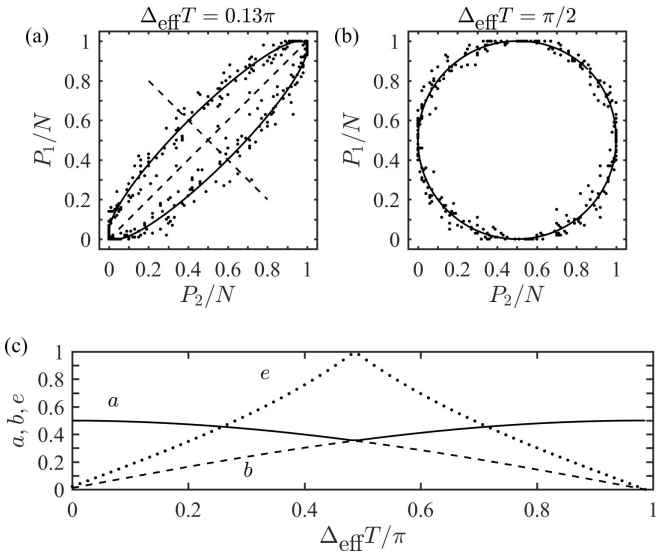

FIG. 2. Synchronous differential comparison with independent spins. (a) and (b) Parametric plots of the excitation fraction of two pixels for different $\Delta_{\rm eff}T$. (Symbols) Monte Carlo simulation. (Solid lines) Analytical results. (c) Dependence of the lengths of half-major a (solid) and half-minor b (dashed) axes and the ellipticity $e = b/a$ (dotted) on $\Delta_{\rm eff}T$.

measurement is determined by the standard deviation $\Delta P_d = \sqrt{\langle \hat{P}_d^2\rangle - \langle \hat{P}_d\rangle^2}$ of P_d,

$$\sigma(\Delta_{\rm eff}) = \frac{2\Delta P_d}{NT} = \frac{2}{NT}\sqrt{(\Delta P_1)^2 + (\Delta P_2)^2 - 2G(P_1, P_2)}, \quad (3)$$

where we have defined the correlation function,

$$G(P_1, P_2) = \langle \hat{P}_1\hat{P}_2\rangle - \langle \hat{P}_1\rangle\langle \hat{P}_2\rangle. \quad (4)$$

Actually, Eq. (3) represents the sensitivity of the spatial-shift measurement. For independent spins, two pixels are uncorrelated and one has $G(P_1, P_2) = 0$. We neglect all technical noise sources. The standard deviation of the Ramsey measurement is then completely caused by the quantum projection noise, $\Delta P_1 = \Delta P_2 = \frac{\sqrt{N}}{2}$ [34], and we obtain

$$\sigma(\Delta_{\rm eff}) = \frac{1}{T}\sqrt{\frac{2}{N}}. \quad (5)$$

Extending the free-evolution time T suppresses the uncertainty $\sigma(\Delta_{\rm eff})$. Nevertheless, the spin decay aggravates the uncertainty for a large T.

An arbitrary state of the ensemble of independent spins may be written as [35]

$$\psi_{\rm CSS}(\theta, \mathbf{n}) = e^{-i\theta\mathbf{n}\cdot(\hat{\mathbf{J}}_1+\hat{\mathbf{J}}_2)}\psi_0, \quad (6)$$

i.e., rotating the initial state ψ_0 around the axis $\mathbf{n}$ by an angle of θ. The expectation value of the total projection operator is $P = \langle \hat{P}\rangle = N(1 - \cos\theta)$ and the corresponding standard deviation is $\Delta P = \sqrt{N/2}|\sin\theta|$. The $\psi_{\rm CSS}(\theta, \mathbf{n})$ state is usually referred to as the coherent spin state (CSS), in which the standard deviation ΔP of the quantum projection noise scales as $\sqrt{N}$, i.e., the standard quantum limit [36]. For the Ramsey measurement, the spin system is in $\psi_{\rm CSS}(\theta = \frac{\pi}{2}, \mathbf{n} = \mathbf{e}_x)$ before the second light $\frac{\pi}{2}$-pulse is launched.

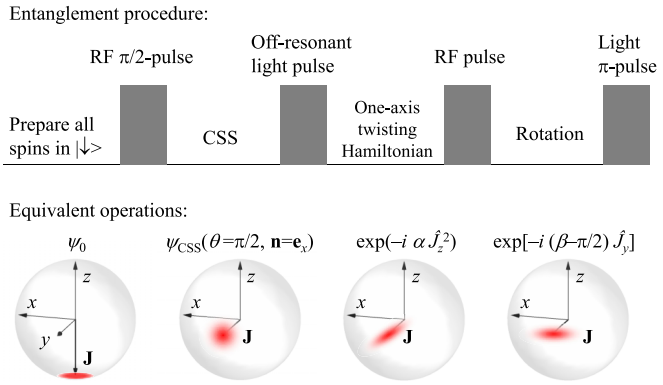

FIG. 3. Procedure of creating entangled spins. (Upper panel) The sequence of RF and light pulses driving the $|\downarrow\rangle - |u\rangle$, $|u\rangle - |v\rangle$, and $|u\rangle - |\uparrow\rangle$ transitions in Fig. 1. (Lower panel) The equivalent operations performed on the spin system.

IV. ENTANGLED SPIN SYSTEM

It has been pointed out that the standard quantum limit may be overcome by employing entangled (correlated) spins [37,38]. Various methods of generating the entanglement between atoms have been proposed [39–41] and demonstrated [28,42,43]. Here, we follow the approach based on the one-axis twisting Hamiltonian [28,40]. Equations (2) and (3) are still valid for entangled spins. As we will see below, the resultant nonzero interpixel correlation $G(P_1, P_2)$ may suppress the deviation ΔP_d of the Ramsey excitation difference below the standard quantum limit.

To create entangled atoms, two auxiliary states, $|u\rangle = (6s^2)\ ^1{\rm S}_0(F = \frac{1}{2}, M_F = \frac{1}{2})$ and $|v\rangle = (6s6p)\ ^3{\rm P}_1(F = \frac{3}{2}, M_F = \frac{3}{2})$, are involved (see Fig. 1), where $|u\rangle$ acts as a role similar to $|\uparrow\rangle$. The specific procedure is summarized as follows (see Fig. 3): All spins are initialized in $|\downarrow\rangle$. A radiofrequency (RF) $\frac{\pi}{2}$-pulse is used to create a CSS between $|\downarrow\rangle$ and $|u\rangle$. This step is equivalent to preparing the spin system in $\psi_{\rm CSS}(\theta = \frac{\pi}{2}, \mathbf{n} = \mathbf{e}_x)$. Subsequently, an off-resonant light pulse drives the $|u\rangle - |v\rangle$ transition through the optical cavity, introducing the cavity-mediated interactions between atoms. This step corresponds to the evolution of the spin system under the one-axis twisting Hamiltonian $\hat{J}_z^2 = (\hat{J}_{z,1} + \hat{J}_{z,2})^2$ for a duration α. Usually, the spin-echo technique is used to eliminate the acquired linear phase shift [28]. Then, another RF pulse is applied to rotate the system composed of $|\downarrow\rangle$ and $|u\rangle$ around the y axis by an angle $(\beta - \frac{\pi}{2})$, equivalent to imposing the same operation on the spin system. Finally, a light π-pulse is launched to map the population in $|u\rangle$ to $|\uparrow\rangle$. In theory, the whole procedure is described as

$$\psi_{\rm SSS1}(\alpha, \beta) = e^{-i(\beta-\pi/2)(\hat{J}_{y,1}+\hat{J}_{y,2})}e^{-i\alpha(\hat{J}_{z,1}+\hat{J}_{z,2})^2} \times \psi_{\rm CSS}(\theta = \pi/2, \mathbf{n} = \mathbf{e}_x). \quad (7)$$

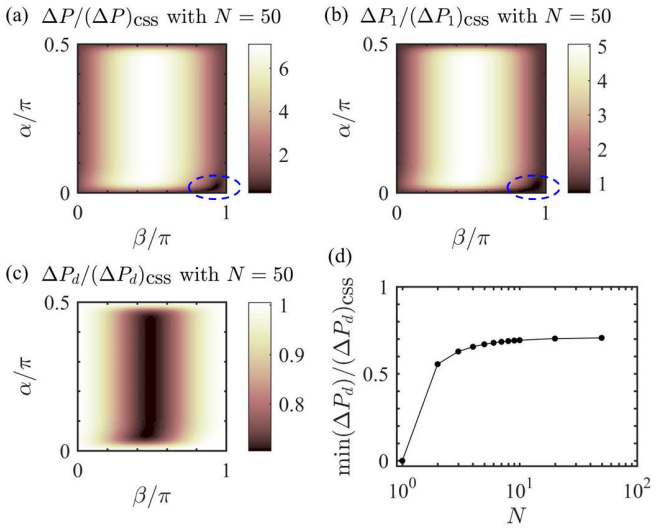

FIG. 4. Standard deviations ΔP (a), $\Delta P_1 = \Delta P_2$ (b), and ΔP_d (c) of entangled spins as a function of the angles α and β with the atom number $N = 50$ of each pixel. The dashed circles in (a) and (b) show the small regimes where $\Delta P < (\Delta P)_{\rm CSS}$ and $\Delta P_{k=1,2} < (\Delta P_k)_{\rm CSS}$, respectively. (d) Dependence of the minimum of ΔP_d on N.

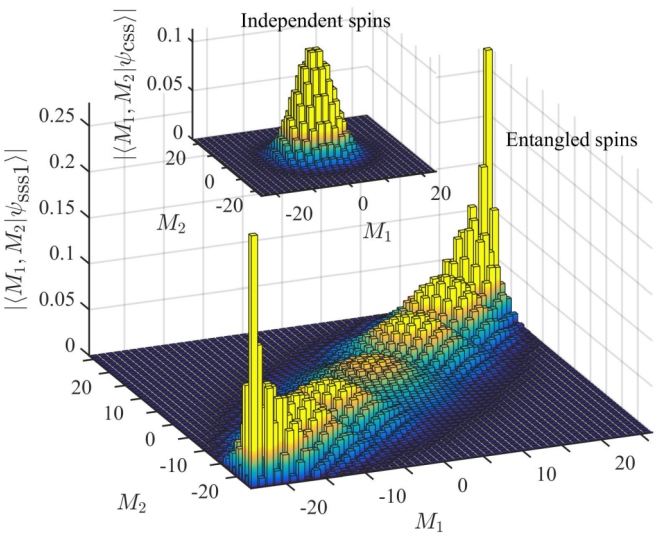

FIG. 5. Population of the entangled $\psi_{\rm SSS1}$ state in different $|M_1, M_2\rangle$ states. Here, $\psi_{\rm SSS1}$ is the state in which $\Delta P_d/(\Delta P_d)_{\rm CSS}$ is minimized. The atom number of each pixel is $N = 50$. (Inset) Population distribution for independent spins, i.e., the spin system is in $\psi_{\rm CSS}(\theta = \frac{\pi}{2}, \mathbf{n} = \mathbf{e}_x)$.

After using the second light $\frac{\pi}{2}$-pulse, one may evaluate the Ramsey excitation refractions of two pixels. It is worth noting that unlike the application of entangled spins in quantum metrology [28,35], the spin entanglement here is employed to suppress the standard deviation ΔP_d of the excitation difference P_d between two pixels so as to reduce the measurement uncertainty $\sigma(\Delta_{\rm eff})$ of the spatial shift $\Delta_{\rm eff}$. Equation (7) is referred to as the squeezed spin state (SSS).

Figure 4(a) plots the deviation $\Delta P = \sqrt{\langle \hat{P}^2\rangle - \langle \hat{P}\rangle^2}$ of the total projection operation $\hat{P}$ (i.e., the Ramsey excitation of the whole spin system) as a function of the angles α and β. It is found that within the most (α, β) regime, ΔP exceeds the corresponding standard quantum limit $(\Delta P)_{\rm CSS} = \sqrt{N/2}$. That is, the entanglement does not always suppress the projection noise. Nevertheless, there is a certain (α, β) regime, within which one has $\Delta P < (\Delta P)_{\rm CSS}$. This is because, according to the Heisenberg uncertainty relation for angular momentum operators, the spreading of the quantum uncertainty in one direction is accompanied by squeezing in the orthogonal axis [35]. In addition, since individual pixels are parts of the whole entangled spin system, the dependence of $\Delta P_{k=1,2} = \sqrt{\langle \hat{P}_k^2\rangle - \langle \hat{P}_k\rangle^2}$ on (α, β) is similar to that of ΔP [see Fig. 4(b)].

Our goal is to reduce the deviation ΔP_d of the excitation difference P_d [see Eq. (3)], rather than the suppression of ΔP or $\Delta P_{k=1,2}$. Interestingly, as shown in Fig. 4(c), ΔP_d is always less than or equal to the standard quantum limit $(\Delta P_d)_{\rm CSS} = \sqrt{N/2}$. This is attributed to the non-negative correlation between two pixels, $G(P_1, P_2) \geqslant 0$ [see Eq. (4)]. Comparing Figs. 4(b) and 4(c), one finds that the strong suppression of ΔP_d occurs within the (α, β) regime where $\Delta P_{k=1,2}$ are strongly enhanced. Thus, despite the strong quantum fluctuations in the Ramsey measurement of individual pixels, the large interpixel correlation (i.e., the entanglement between two pixels) still ensures the suppression of the quantum noise in the synchronous differential measurement.

In the special case, where each pixel contains only one spin, i.e., $N = 1$, the minimum of ΔP_d reaches zero, i.e., $\min(\Delta P_d) = 0$ [see Fig. 4(d)]. Actually, this situation is analogous to the recent experiment in [27], where two single ion clocks are fully entangled, i.e., $\psi_{\rm SSS1} = \frac{1}{\sqrt{2}}(|M_1 = -\frac{1}{2}, M_2 = -\frac{1}{2}\rangle + |M_1 = \frac{1}{2}, M_2 = \frac{1}{2}\rangle)$. As N is increased, the ratio $\min(\Delta P_d)/(\Delta P_d)_{\rm CSS}$ approaches a saturation value of $\sim$0.7, corresponding to a metrological gain of 1.5 decibels and a reduction of the averaging time by a factor of 2. The saturation indicates that both $\min(\Delta P_d)$ and $(\Delta P_d)_{\rm CSS}$ scale as $\sqrt{N}$ for a large N, i.e., the entanglement based on $\psi_{\rm SSS1}$ does not change the scaling. Here, $\psi_{\rm SSS1}$ corresponds to the entangled state in which $\Delta P_d/(\Delta P_d)_{\rm CSS}$ reaches its minimum.

In order to gain insight into the entanglement between two pixels, we compute the distribution of the entangled $\psi_{\rm SSS1}$ state in different $|M_1, M_2\rangle$ states. As depicted in Fig. 5, the entangled spin system is mainly populated around the diagonal line with $M_1 = M_2$ in the (M_1, M_2) regime. In contrast, the system composed of independent spins is mainly populated around $|M_1 = 0, M_2 = 0\rangle$ and the distribution presents an isotropic Gaussian pattern (see the inset in Fig. 5), indicating the single spin behavior. Thus, the entanglement synchronizes the excitations of two pixels. Additionally, the distribution of $\psi_{\rm SSS1}$ is maximized at the $|M_1 = \frac{N}{2}, M_2 = \frac{N}{2}\rangle$ and $|M_1 = -\frac{N}{2}, M_2 = -\frac{N}{2}\rangle$ states, characterizing the cooperative behavior of spins. The resulting correlation $G(P_1, P_2)$ has the same scaling $(\propto N)$ with $(\Delta P_{k=1,2})^2$ for a large N, leading to $\min(\Delta P_d) \propto \sqrt{N}$. According to the distribution shown in Fig. 5, one may numerically simulate the Ramsey excitation fractions $P_{1,2}$ of two pixels by using the Monte Carlo method.

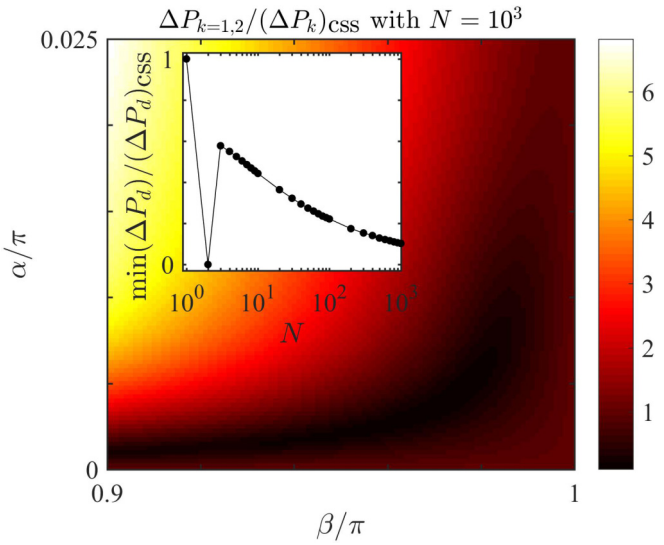

FIG. 6. Dependence of the deviation $\Delta P_{k=1,2}$ on the angles α and β, where the system is in $\psi_{\rm SSS2}(\alpha, \beta)$ before the second light $\frac{\pi}{2}$-pulse is launched in the Ramsey measurement. The number of the spins in each pixel is $N = 10^3$. (Inset) The ratio of the minimum of ΔP_d to $(\Delta P_d)_{\rm CSS}$ changing with N.

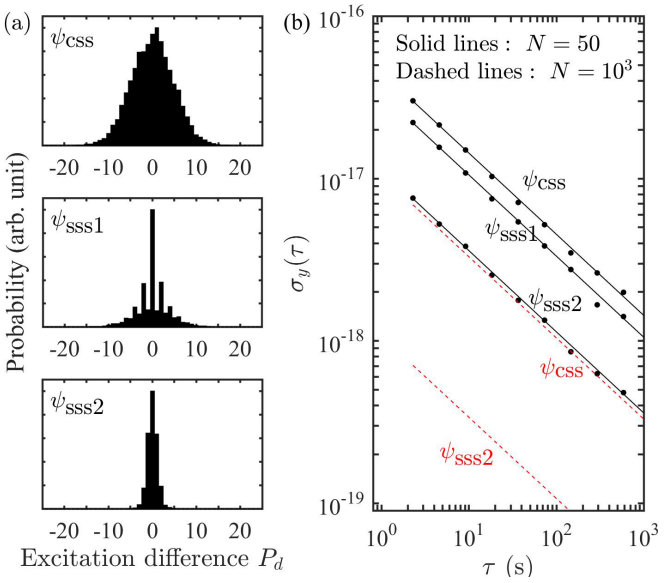

FIG. 7. Monte Carlo simulation. (a) Distributions of the Ramsey excitation difference P_d between two pixels for the spin system in different states. For all plots, the spin number is $N = 50$. (b) Allan deviation $\sigma_y(\tau)$ of the synchronous differential measurement of the spatial shift $\Delta_{\rm eff}$. (Symbols) Numerical results with $N = 50$. (Solid lines) Curve fitting. (Dashed line) Analytical results with $N = 10^3$.

V. TWO INDEPENDENT PIXELS WITH EACH INDIVIDUAL COMPOSED OF ENTANGLED SPINS

In the last section, we have discussed the synchronous comparison with the entanglement of all spins, where the positive interpixel correlation reduces the deviation ΔP_d of the Ramsey excitation difference P_d. From Eq. (3), it is seen that ΔP_d can be also suppressed by reducing $\Delta P_{1,2}$ even when the interpixel correlation $G(P_1, P_2)$ vanishes, i.e., $\Delta P_d = \sqrt{2}\Delta P_1 < (\Delta P_d)_{\rm CSS}$. Here, we have used $\Delta P_1 = \Delta P_2$. Motivated by this, we further consider the following situation, where two pixels are independent while the spins in each pixel are entangled through the approach shown in Fig. 3. Thus, the system is in

$$\psi_{\rm SSS2}(\alpha, \beta) = \prod_{k=1,2} e^{-i(\beta-\pi/2)\hat{J}_{y,k}} e^{-i\alpha\hat{J}^2_{z,k}} \times \psi_{\rm CSS}(\theta = \pi/2, \mathbf{n} = \mathbf{e}_x), \quad (8)$$

before the second light $\frac{\pi}{2}$-pulse is launched in the Ramsey measurement. Such an entanglement scheme may be implemented by using the optical tweezer clock technique [44–46].

Figure 6 displays the dependence of $\Delta P_{k=1,2}$ on the angles α and β. As is expected, within a certain (α, β) regime the entanglement of spins in each pixel may reduce $\Delta P_{k=1,2}$ below that of the pixels composed of independent spins. The inset in Fig. 6 plots the minimum of the resultant deviation ΔP_d of the Ramsey excitation difference as a function of the number N of spins in each pixel. In the simplest case with $N = 1$, one has $\Delta P_d = (\Delta P_d)_{\rm CSS}$. For $N = 2$, the squeezed $\psi_{\rm SSS2}$ state takes the form of $|\Phi\rangle_1 \otimes |\Phi\rangle_2$ with the Bell state $|\Phi\rangle_k = \frac{1}{\sqrt{2}}(|\downarrow\downarrow\rangle - |\uparrow\uparrow\rangle)_k$ of the kth pixel and the minimum of ΔP_d reaches zero. Recently, the enhanced metrological stability has been demonstrated by using the long-lived Bell states [26]. Unlike the system in $\psi_{\rm SSS1}$, increasing the spin number N may further suppress the ratio $\min(\Delta P_d)/(\Delta P_d)_{\rm CSS}$ for the system in $\psi_{\rm SSS2}$ [see Fig. 4(d) and the inset in Fig. 6]. For example, $\psi_{\rm SSS2}$ leads to $\min(\Delta P_d)/(\Delta P_d)_{\rm CSS} \approx 0.27$ (0.1) when $N = 50$ (10^3), corresponding to a spatial-shift sensitivity enhancement of 5.7 (9.9) decibels. This is attributed to the fact that for the system in $\psi_{\rm SSS2}$ the squeezed $\Delta P_{k=1,2}$ scale as N^ν with $\nu < \frac{1}{2}$.

VI. ALLAN DEVIATION

Finally, we consider the stability (i.e., Allan deviation) of the synchronous differential measurement of the spatial shift $\Delta_{\rm eff}$. We numerically simulate the pixel populations $P_{1,2}$ using the Monte Carlo method (see Appendix A) and compute the Ramsey excitation difference P_d. Figure 7(a) shows the distributions of P_d for the spin system in $\psi_{\rm CSS}$, $\psi_{\rm SSS1}$, and $\psi_{\rm SSS2}$, respectively. It is seen that the $\psi_{\rm CSS}$ state leads to a Gaussian distribution of P_d with the standard deviation of $\Delta P_d = \sqrt{N/2}$. In contrast, P_d for the system in $\psi_{\rm SSS1}$ has a distribution width narrower than that of $\psi_{\rm CSS}$. The distribution width is further narrowed when the system is in $\psi_{\rm SSS2}$.

According to Eq. (2), one may compute the spatial shift $\Delta_{\rm eff}$ from the measurement of P_d. This $\Delta_{\rm eff}$ corresponds to the mean value of the spatial shift averaged over a cycle time T_c. Each cycle is composed of the preparation of lattice-trapped spins (i.e., laser cooling and trapping, loading atoms into the optical lattice, and Raman sideband cooling), the generation of the entanglement between spins (i.e., optically pumping spins into $|\downarrow\rangle$, creating CSS, evolving under the one-axis twisting Hamiltonian, and rotating SSS), and the Ramsey measurement (i.e., Ramsey sequence and interrogation of spins). Typically, the Ramsey free evolution time T is of the order of 1 s and the total time duration for preparing lattice-trapped spins, creating entangled spins, and the state measurement is of the order of 0.1 s [28]. Thus, T_c approximates T.

Performing the simulation repeatedly, one obtains a frequency series $\{\Delta_{\mathrm{eff},k}, k \in Z\}$, where the index k denotes the kth measurement cycle. The Allan deviation is then given by

$$\sigma_y(\tau = nT_c) = \omega_0^{-1}\sqrt{\langle(\bar{\Delta}_{\mathrm{eff},m+1} - \bar{\Delta}_{\mathrm{eff},m})^2\rangle}, \tag{9}$$

with $\bar{\Delta}_{\mathrm{eff},m} = \frac{1}{n}\sum_{k=(m-1)n+1}^{mn}\Delta_{\mathrm{eff},k}$ averaged over the period and $n \in Z$.

The numerical results with $T = 2$ s and $T_c = 2.3$ s [28] are shown in Fig. 7(b). The entanglement of spins improves the stability of the measurement of Δ_{eff}. For $N = 50$, the Allan deviation for the system in ψ_{CSS} is evaluated to be $\sigma_y(\tau) = 4.5\times10^{-17}/\sqrt{\tau}$. Preparing the system in ψ_{SSS1} leads to $\sigma_y(\tau) = 3.3\times10^{-17}/\sqrt{\tau}$. In contrast, the Allan deviation for the system in ψ_{SSS2} is $\sigma_y(\tau) = 1.1\times10^{-17}/\sqrt{\tau}$, denoting a metrological gain of 6.1 decibels over the standard quantum limit and a reduction of the averaging time by a factor greater than 16. The analytic expression of the Allan deviation takes the form,

$$\begin{aligned}\sigma_y(\tau) &= \frac{\sigma(\Delta_{\mathrm{eff}})}{\omega_0}\sqrt{\frac{T_c}{\tau}} \\ &= \frac{2\Delta P_d/N}{\omega_0 T}\sqrt{\frac{T_c}{\tau}}.\end{aligned} \tag{10}$$

Since ΔP_d for the system in ψ_{SSS2} decreases with the atom number N (see the inset in Fig. 6), one may increase N to enhance the measurement stability. When $N = 10^3$, we obtain $\sigma_y(\tau) = 1.0\times10^{-18}/\sqrt{\tau}$, improved by a factor of 4 compared to the one in [24], by employing ψ_{SSS2} [see Fig. 7(b)]. For two pixels with an effective separation of 20 μm, the gravitational redshift at the Earth's surface causes a fractional frequency difference of 2.2×10^{-21}, which can be resolved when $\tau \approx$ 60 h.

VII. CONCLUSION

In summary, we have investigated the application of the entanglement of atoms in the synchronous differential comparison. The resultant suppression of the deviation of Ramsey excitation difference between two pixels leads to an enhanced sensitivity of the spatial-shift detection and a strong reduction of the averaging time. The proposed metrology scheme is feasible by means of the recent atom-optical techniques and will advance tests of fundamental physics.

In this study, we have assumed two pixels have the same atom number. However, in practice this cannot be ensured when preparing the sample. In addition, the total number of atoms varies for different samples. According to the experiment in [28], the standard deviation σ_N of the atom number whose mean value is $N = 350$ can be controlled to $\sigma_N = 40$. In contrast, the experiment in [20] has $N \approx 10^3$ with σ_N of the order of 10. Assuming a deviation of $\sigma_N/N = 0.01$, we estimate that the fluctuations of the atom number cause an extra uncertainty component in $\sigma(\Delta_{\mathrm{eff}})$ less than one percent.

Note added. Recently, we became aware of the experiment of the direct comparison of two spin squeezed optical clocks [47].

ACKNOWLEDGMENT

D.Y. acknowledges the funding provided by National Time Service Center, China (Grant No. E239SC11).

APPENDIX: RAMSEY MEASUREMENT

We simulate the Ramsey measurement on an ensemble of N spins. In the Heisenberg picture, one has the projection operator,

$$\begin{aligned}\hat{P}(\phi) &= N/2 + e^{i\pi\hat{J}_x/2}e^{-i\phi\hat{J}_z/2}e^{i\pi\hat{J}_x/2}\hat{J}_z \\ &\quad\times e^{-i\pi\hat{J}_x/2}e^{i\phi\hat{J}_z/2}e^{-i\pi\hat{J}_x/2} \\ &= N/2 - \hat{J}_z\cos\phi - \hat{J}_x\sin\phi.\end{aligned} \tag{A1}$$

Here, ϕ is the phase difference between two light $\frac{\pi}{2}$-pulses. The expectation value of $\hat{P}(\phi)$ is given by $P(\phi) = \langle\hat{P}(\phi)\rangle = \langle\psi|\hat{P}(\phi)|\psi\rangle$ with the initial state ψ of the system. The standard deviation $\Delta P = \sqrt{\langle\hat{P}^2\rangle - \langle\hat{P}\rangle^2}$ of the projection measurement takes the form,

$$\begin{aligned}(\Delta P)^2 &= (\langle\hat{J}_z\hat{J}_x\rangle + \langle\hat{J}_x\hat{J}_z\rangle - 2\langle\hat{J}_z\rangle\langle\hat{J}_x\rangle)\cos\phi\sin\phi \\ &\quad + (\Delta J_z)^2\cos^2\phi + (\Delta J_x)^2\sin^2\phi,\end{aligned} \tag{A2}$$

with $\Delta J_{u=x,z} = \sqrt{\langle\hat{J}_u^2\rangle - \langle\hat{J}_u\rangle^2}$. For independent atoms, the standard deviation $\Delta P/\sqrt{N}$ reaches zero when $P/N = 0$ or $P/N = 1$, i.e., all spins are in $|\downarrow\rangle$ or $|\uparrow\rangle$, and is maximized when $P/N = 1/2$.

One may also compute the distribution $p(M) = |\langle J = N/2, M|\psi(\phi)\rangle|^2$ of spins in different states. Here $\psi(\phi)$ is the wave function of the system after the second light $\frac{\pi}{2}$-pulse is launched. We have $P = \sum_M(M + \frac{N}{2})p(M)$ and $(\Delta P)^2 = \sum_M(M + \frac{N}{2})^2p(M) - P^2$. According to $p(M)$, one can numerically simulate the spin excitation through the Monte Carlo method. For a certain ϕ, we need to select a specific $(M + \frac{N}{2})$ with the corresponding probability $p(M)$ as a Ramsey measurement result. To this end, we compute the maximum $p_{\max}$ in the array $\{p(-J), p(-J+1), \cdots, p(J-1), p(J)\}$, shuffle the elements in the array, and draw a uniform random number x in [0,1]. Then, we compare x to the first element $p(\tilde{M})$ in the shuffled array. If $x < \frac{p(\tilde{M})}{p_{\max}}$, the Ramsey measurement result is $(\tilde{M} + \frac{N}{2})$. Otherwise, the procedure is repeated. Finally, one obtains an ensemble of measurement results, whose mean value is P and standard deviation is ΔP.

[1] C. W. Chou, D. B. Hume, J. C. J. Koelemeij, D. J. Wineland, and T. Rosenband, Phys. Rev. Lett. **104**, 070802 (2010).

[2] N. Hinkley, J. A. Sherman, N. B. Phillips, M. Schioppo, N. D. Lemke, K. Beloy, M. Pizzocaro, C. W. Oates, and A. D. Ludlow, Science **341**, 1215 (2013).

[3] B. J. Bloom, T. L. Nicholson, J. R. Williams, S. L. Campbell, M. Bishof, X. Zhang, W. Zhang, S. L. Bromley, and J. Ye, Nature (London) **506**, 71 (2014).

[4] I. Ushijima, M. Takamoto, M. Das, T. Ohkubo, and H. Katori, Nat. Photon. **9**, 185 (2015).

[5] N. Huntemann, C. Sanner, B. Lipphardt, Chr. Tamm, and E. Peik, Phys. Rev. Lett. **116**, 063001 (2016).

[6] T. Bothwell, D. Kedar, E. Oelker, J. M. Robinson, S. L. Bromley, W. L. Tew, J. Ye, and C. J. Kennedy, Metrologia **56**, 065004 (2019).

[7] N. Huntemann, B. Lipphardt, Chr. Tamm, V. Gerginov, S. Weyers, and E. Peik, Phys. Rev. Lett. **113**, 210802 (2014).

[8] R. M. Godun, P. B. R. Nisbet-Jones, J. M. Jones, S. A. King, L. A. M. Johnson, H. S. Margolis, K. Szymaniec, S. N. Lea, K. Bongs, and P. Gill, Phys. Rev. Lett. **113**, 210801 (2014).

[9] P. Kómór, E. M. Kessler, M. Bishof, L. Jiang, A. S. Sørensen, J. Ye, and M. D. Lukin, Nat. Phys. **10**, 582 (2014).

[10] T. Takano, M. Takamoto, I. Ushijima, N. Ohmae, T. Akatsuka, A. Yamaguchi, Y. Kuroishi, H. Munekane, B. Miyahara, and H. Katori, Nat. Photon. **10**, 662 (2016).

[11] C. Lisdat *et al.*, Nat. Commun. **7**, 12443 (2016).

[12] R. B. Hutson, A. Goban, G. E. Marti, L. Sonderhouse, C. Sanner, and J. Ye, Phys. Rev. Lett. **123**, 123401 (2019).

[13] A. Aeppli, A. Chu, T. Bothwell, C. J. Kennedy, D. Kedar, P. He, A. M. Rey, and J. Ye, Sci. Adv. **8**, eadc9242 (2022).

[14] M. D. Swallows, M. N. Bishof, Y. Lin, S. Blatt, M. J. Martin, A. M. Rey, and J. Ye, Science **331**, 1043 (2011).

[15] M. Takamoto, I. Ushijima, N. Ohmae, T. Yahagi, K. Kokado, H. Shinkai, and H. Katori, Nat. Photon. **14**, 411 (2020).

[16] G. Santarelli, C. Audoin, A. Makdissi, P. Laurent, G. J. Dick, and A. Clairon, IEEE Trans. Ultrason. Ferroelectr. Freq. Control **45**, 887 (1998).

[17] T. Kessler, C. Hagemann, C. Grebing, T. Legero, U. Sterr, F. Riehle, M. J. Martin, L. Chen, and J. Ye, Nat. Photon. **6**, 687 (2012).

[18] J. M. Robinson, E. Oelker, W. R. Milner, W. Zhang, T. Legero, D. G. Matei, F. Riehle, U. Sterr, and J. Ye, Optica **6**, 240 (2019).

[19] D. G. Matei, T. Legero, S. Häfner, C. Grebing, R. Weyrich, W. Zhang, L. Sonderhouse, J. M. Robinson, J. Ye, F. Riehle, and U. Sterr, Phys. Rev. Lett. **118**, 263202 (2017).

[20] M. Takamoto, T. Takano, and H. Katori, Nat. Photon. **5**, 288 (2011).

[21] M. Schioppo, R. C. Brown, W. F. McGrew, N. Hinkley, R. J. Fasano, K. Beloy, T. H. Yoon, G. Milani, D. Nicolodi, J. A. Sherman, N. B. Phillips, C. W. Oates, and A. D. Ludlow, Nat. Photon. **11**, 48 (2017).

[22] E. Oelker, R. B. Hutson, C. J. Kennedy, L. Sonderhouse, T. Bothwell, A. Goban, D. Kedar, C. Sanner, J. M. Robinson, G. E. Marti, D. G. Matei, T. Legero, M. Giunta, R. Holzwarth, F. Riehle, U. Sterr, and J. Ye, Nat. Photon. **13**, 714 (2019).

[23] X. Zheng, J. Dolde, V. Lochab, B. N. Merriman, H. Li, and S. Kolkowitz, Nature (London) **602**, 425 (2022).

[24] T. Bothwell, C. J. Kennedy, A. Aeppli, D. Kedar, J. M. Robinson, E. Oelker, A. Staron, and J. Ye, Nature (London) **602**, 420 (2022).

[25] M. Schulte, C. Lisdat, P. O. Schmidt, U. Sterr, and K. Hammerer, Nat. Commun. **11**, 5955 (2020).

[26] N. Schine, A. W. Young, W. J. Eckner, M. J. Martin, and A. M. Kaufman, Nat. Phys. **18**, 1067 (2022).

[27] B. C. Nichol, R. Srinivas, D. P. Nadlinger, P. Drmota, D. Main, G. Araneda, C. J. Ballance, and D. M. Lucas, Nature (London) **609**, 689 (2022).

[28] E. Pedrozo-Peñafiel, S. Colombo, C. Shu, A. F. Adiyatullin, Z. Li, E. Mendez, B. Braverman, A. Kawasaki, D. Akamatsu, Y. Xiao, and V. Vuletić, Nature (London) **588**, 414 (2020).

[29] P. Wcisło *et al.*, Sci. Adv. **4**, eaau4869 (2018).

[30] S. Kolkowitz, I. Pikovski, N. Langellier, M. D. Lukin, R. L. Walsworth, and J. Ye, Phys. Rev. D **94**, 124043 (2016).

[31] Q. Gao, M. Zhou, C. Han, S. Li, S. Zhang, Y. Yao, B. Li, H. Qiao, D. Ai, G. Lou, M. Zhang, Y. Jiang, Z. Bi, L. Ma, and X. Xu, Sci. Rep. **8**, 8022 (2018).

[32] G. E. Marti, R. B. Hutson, A. Goban, S. L. Campbell, N. Poli, and J. Ye, Phys. Rev. Lett. **120**, 103201 (2018).

[33] S. G. Porsev, A. Derevianko, and E. N. Fortson, Phys. Rev. A **69**, 021403(R) (2004).

[34] W. M. Itano, J. C. Bergquist, J. J. Bollinger, J. M. Gilligan, D. J. Heinzen, F. L. Moore, M. G. Raizen, and D. J. Wineland, Phys. Rev. A **47**, 3554 (1993).

[35] J. Ma, X. Wang, C. P. Sun, and F. Nori, Phys. Rep. **509**, 89 (2011).

[36] G. Santarelli, Ph. Laurent, P. Lemonde, A. Clairon, A. G. Mann, S. Chang, A. N. Luiten, and C. Salomon, Phys. Rev. Lett. **82**, 4619 (1999).

[37] D. J. Wineland, J. J. Bollinger, W. M. Itano, F. L. Moore, and D. J. Heinzen, Phys. Rev. A **46**, R6797 (1992).

[38] D. J. Wineland, J. J. Bollinger, W. M. Itano, and D. J. Heinzen, Phys. Rev. A **50**, 67 (1994).

[39] M. Kitagawa and M. Ueda, Phys. Rev. A **47**, 5138 (1993).

[40] M. H. Schleier-Smith, I. D. Leroux, and V. Vuletić, Phys. Rev. A **81**, 021804(R) (2010).

[41] M. A. Perlin, C. Qu, and A. M. Rey, Phys. Rev. Lett. **125**, 223401 (2020).

[42] K. Lange, J. Peise, B. Lücke, I. Kruse, G. Vitagliano, I. Apellaniz, M. Kleinmann, G. Tóth, and C. Klempt, Science **360**, 416 (2018).

[43] H. Bao, J. Duan, S. Jin, X. Lu, P. Li, W. Qu, M. Wang, I. Novikova, E. E. Mikhailov, K.-F. Zhao, K. Mølmer, H. Shen, and Y. Xiao, Nature (London) **581**, 159 (2020).

[44] I. S. Madjarov, A. Cooper, A. L. Shaw, J. P. Covey, V. Schkolnik, T. H. Yoon, J. R. Williams, and M. Endres, Phys. Rev. X **9**, 041052 (2019).

[45] M. A. Norcia, A. W. Young, W. J. Eckner, E. Oelker, J. Ye, and A. M. Kaufman, Science **366**, 93 (2019).

[46] J. P. Covey, I. S. Madjarov, A. Cooper, and M. Endres, Phys. Rev. Lett. **122**, 173201 (2019).

[47] J. M. Robinson, M. Miklos, Y. M. Tso, C. J. Kennedy, T. Bothwell, D. Kedar, J. K. Thompson, and J. Ye, arXiv:2211.8621.